Estimation of Thickness and Speed of Sound in Cortical Bone Using Multifocus Pulse-Echo Ultrasound

Huong Nguyen Minh, *Member, IEEE*, Juan Du, *Member, IEEE*, and Kay Raum, *Member, IEEE*

***Abstract*— Most bone loss during the development of osteoporosis occurs in cortical bone at the peripheral skeleton. Decreased cortical thickness (*Ct.Th*) and the prevalence of large pores at the tibia are associated with reduced bone strength at the hip. *Ct.Th* and cortical sound velocity, i.e., a surrogate marker for changes of cortical porosity (*Ct.Po*), are key biomarkers for the identification of patients at high fracture risk. In this study, we have developed a method using a conventional ultrasound array transducer to determine thickness (*Ct.Th*) and the compressional sound velocity propagating in the radial bone direction ($Ct.v_{11}$) using a refraction-corrected multifocus imaging approach. The method was validated *in-silico* on porous bone plate models using a 2-D finite-difference time-domain method and *ex vivo* on plate-shaped plastic reference materials and on plate-shaped cortical bovine tibia samples. Plane-wave pulse-echo measurements provided reference values to assess precision and accuracy of our method. *In-silico* results revealed the necessity to account for inclination-dependent transmission losses at the bone surface. Moreover, the dependence of $Ct.v_{11}$ on both porosity and pore density was observed. *Ct.Th* and $Ct.v_{11}$ obtained *ex vivo* showed a high correlation ($R2 > 0.99$) with reference values. The *ex-vivo* accuracy and precision for $Ct.v_{11}$ were 29.9 m/s and 0.94%, respectively, and those for *Ct.Th* were 0.04 mm and 1.09%, respectively. In conclusion, this numerical and experimental study demonstrates an accurate and precise estimation of *Ct.Th* and $Ct.v_{11}$. The developed multifocus technique may have high clinical potential to improve fracture risk prediction using noninvasive and nonionizing conventional ultrasound technology with image guidance.**

***Index Terms*— Medical beamforming and beam steering, medical signal and image processing, medical tissue characterization, pulse-echo ultrasound.**

I. Introduction

OSTEOPOROSIS (OP) is one of the most important global health problems of our aging population, which reduces mobility and quality of life, increases mortality, and sets a dramatic burden on the healthcare system [1]. The current gold standard to predict bone status and fracture risk is the measurement of bone mineral density (BMD) by means of dual-energy X-ray absorptiometry (DXA) at major fracture sites, i.e., spine and proximal femur. These measurement regions are predominantly composed of trabecular bone. However, ∼70% of bone loss occurs after age 65 at peripheral sites and is cortical, not trabecular, which contributes ∼80% of the human skeleton and contributes most to bone strength [1], [2]. Unbalanced intracortical remodeling leaves progressively more nonrefilled bone multicellular units (BMUs) in the cortex, which becomes thinner and contains particularly large coalescent basic multicellular units (hereinafter called large BMUs) compared with the Haversian canals. In particular, in the endosteal subcompartment, close clustering of BMUs enhances their chances to merge, leading to the so-called trabecularized cortex [2]. Decreased cortical thickness and the prevalence of large BMU's reduce bone strength [3] and are quantifiable "fingerprints" of structural deterioration [4]. However, cortical bone loss and the resulting structural decay are poorly captured by BMD [5]–[7]. In fact, the majority of individuals who have sustained an OP-related fracture or who are at high risk of fracture are not diagnosed as osteoporotic according to the BMD level [1]. In the past three decades, quantitative ultrasound (QUS) methods have been introduced as nonionizing alternatives for the diagnosis of OP and the prediction of fracture risk. While the early QUS approaches have targeted trabecular sites, e.g., at the heel, and aimed at predicting BMD via empirical associations with the measured speed of sound (SOS) and broadband ultrasound attenuation [8], recent QUS technologies target cortical measurement sites, e.g., distal radius and tibia, and aim at the quantitative assessment of structural cortical bone properties, e.g., cortical thickness *Ct.Th* and cortical porosity *Ct.Po*. One approach proposed by Karjalainen *et al.* [9] uses an unfocused single-element pulse-echo configuration to measure the time delay between waves reflected from the periosteal and endosteal bone interfaces. Using the assumption of a known and invariant radial sound velocity of 3565 m/s, the apparent cortical thickness is derived from the time lag between reflections from the periosteal and endosteal interfaces [10]. The time lag can be determined using autocorrelation, envelope peak detection, or cepstral methods [9], [11]. A multivariable optimization approach was proposed by Tasinkevych *et al.* [12] to determine thickness and compressional wave velocity by fitting experimentally

Manuscript received June 26, 2019; accepted October 16, 2019. Date of publication October 24, 2019; date of current version February 25, 2020. This work was supported in part by the joint ANR-DFG TaCo-Sound Project under Grant DFG RA1380/9-1, Grant GL289/8-1, and Grant ANR-14-CE35-0030-01, and in part by the BMBF KMU-Innovative Project through German Federal Ministry of Education and Research under Grant 13GW0234C. *(Corresponding author: Kay Raum.)*

H. Nguyen Minh and K. Raum are with the Berlin Brandenburg Center for Regenerative Therapies, Charité—Universitätsmedizin Berlin, 10178 Berlin, Germany (e-mail: huong.nguyen-minh@charite.de; kay.raum@charite.de).

J. Du was with the Berlin Brandenburg Center for Regenerative Therapies, Charité—Universitätsmedizin Berlin, 10178 Berlin, Germany. She is now with Digital Endoscopy GmbH, 86316 Friedberg, Germany (e-mail: duxxx134@umn.edu).

Digital Object Identifier 10.1109/TUFFC.2019.2948896

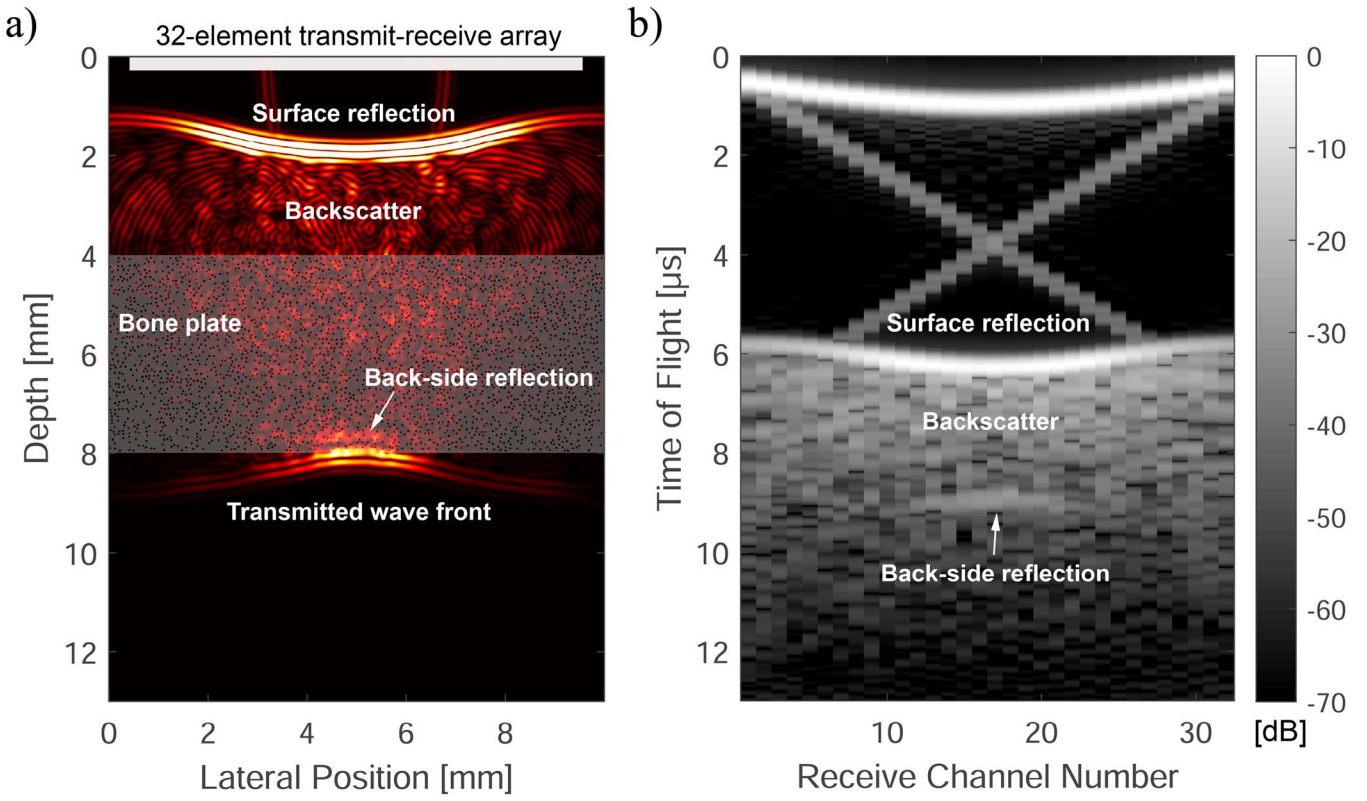

Fig. 1. (a) Snapshot of a numerical simulation model. The bone model contains randomly distributed pores with Po = 9% and Po.Dm = 42.5 μm. (b) Pulse-echo signals (envelope) recorded by the receiver elements. The lateral and temporal increments correspond to the element and pitch sizes of 0.3 mm in the horizontal direction and the temporal sampling increment of 25 ns (after downsampling) in the vertical direction.

measured amplitude and phase spectra of the reflected signals to corresponding simulated spectra. However, the method relies on the assumptions of normal sound incidence on a homogenous material with perfectly flat interfaces and *a priori* knowledge of some material properties, e.g., the attenuation in cortical bone and the reflection coefficient at the bone interfaces. Zheng *et al.* [13] proposed an imaging method of the cortical layer of a bovine tibia bone using a Born-based inversion scattering technique to reconstruct the wave path and to estimate the cortical thickness. The method was demonstrated *ex vivo* on one bovine tibia, but no velocity and thickness values derived from this approach were reported. The combined estimation of cortical thickness and porosity has been achieved by means of full-wave dispersion analysis of guided waves in axial transmission measurements [14]. This method relies on the assumptions as: 1) wave dispersion in long bones can be approximated by a free plate model and 2) that variations of the elastic stiffness tensor at the mm-length scale can be entirely described by the volume fraction of pores pervading the extracellular matrix [15]. However, the application of axial transmission measurements is restricted to patients with low body mass index [16], [17]. Among other reasons, the lack of a direct image-guided measurement results in a high-operator dependence, and underlying assumptions for the parameter estimation may not always be fulfilled. Refraction-corrected bone imaging approach using single-element transmission, and full-array waveform capture has been proposed by Renaud *et al.* [18]. This method provides images of the periosteal and endosteal bone interfaces and estimates both cortical thickness and an anisotropic sound velocity profile.

The objective of this study was to develop a method that uses conventional, multielement transmit and receive array imaging technology and a refraction-corrected multifocus imaging approach to determine cortical thickness *Ct.Th* and the velocity of the compressional wave propagating in radial bone direction ($Ct.v_{11}$). The method has been validated: 1) *in silico* by means of finite-difference time-domain (FDTD) simulations in academic bone plate models with random microstructures of variable pore sizes and densities and 2) experimentally on nonporous polymer reference material plates and on porous bovine bone plates. Note that for consistency, the variables *Ct.Th* and $Ct.v_{11}$ are used hereinafter for sample thickness and sound velocity, even if the samples were not cortical bone.

II. Materials and Methods

A. Numerical Ultrasound Propagation Model

Ultrasound wave propagation in water and bone was simulated using the 2-D FDTD method with Simsonic (www.simsonic.fr) [19]. The elastic simulation model considers multiple scattering, frequency-independent absorption, refraction, diffraction, and wave conversion, which occurs during the wave propagation in a bone. Our model geometry consists of a 4-mm-thick bone plate immersed in water Fig. 1(a)]. Randomly distributed circular pores resemble

TABLE I
TISSUE MATERIAL PROPERTIES OF BONE AND PORES USED FOR THE NUMERICAL MODEL. MASS DENSITY ρ AND c_{ij}, I.E., THE COEFFICIENTS OF A TRANSVERSE ISOTROPIC STIFFNESS TENSOR WERE OBTAINED FROM [20] AND THE ABSORPTION VALUE α WAS TAKEN FROM [21]

	BONE	PORES
ρ [g/cm^3]	1.93	1.00
c_{11} [GPa]	23.7	2.25
c_{22} [GPa]	23.7	2.25
c_{12} [GPa]	9.5	2.25
c_{66} [GPa]	6.6	0
v_{11} [m/s]	3504	1500
α [dB/mm]	2.1	0.002

Haversian canals intersecting the image plane. Perfectly matched layers (width: 300 pixels and attenuation: 160 dB) were added at all edges of the map. Material properties for the extracellular bone matrix in human cortical bone are considered to be transverse isotropic [20], with the plane of symmetry parallel to the image plane. The simulation was performed in the isotropic plane with wave propagations in the radial bone direction. Material properties were used from a previous acoustic microscopy study in a human femur [20] and an *ex-vivo* study [21] and are summarized in Table I. A convergence study provided stable results for spatial and temporal grid sizes of 7 µm and 0.93 ns, respectively.

The bone plate was placed 4 mm below the transducer, i.e., a linear array with 32 elements (element and pitch sizes: 0.3 mm). Elements emitted broadband pulses with a center frequency of 5 MHz and a −6-dB bandwidth of 60%. Phase delays were applied to focus the transmit beam subsequently to focus depths of −24 mm with an increment of 1 mm [Fig. 1(a)]. The signals received at all elements were recorded and downsampled to a sampling rate of 80 MHz for further processing [Fig. 1(b)]. Recent *ex-vivo* studies in human cortical bone reported *Ct.Po* and cortical pore diameter (*Ct.Po.Dm*), defined as the diameter of single Haversian canals or BMU's with a circular shape, values between 2% and 22%, and 7 and 95 μm, respectively [3], [22], [23]. Therefore, two groups were modeled by varying either porosity or pore size: mode I: $Ct.Po.Dm = 38.6$ μm; $Ct.Po \in$ [0%–20%; step size: 2%], cortical pore density $Ct.Po.Dn \in$ [0 mm^{-2}–140 mm^{-2}; step size: 14 mm^{-2}]; and model II: $Ct.Po = 10\%$; $Ct.Po.Dm \in$ [17.7–96.3 μm; variable step size], $Ct.Po.Dn \in$ [408 mm^{-2}–13.7 mm^{-2}; nonlinear decrease with increasing *Ct.Po.Dm*]. Each bone model was generated six times.

B. Sample Collection, Preparation, and Reference Thickness Measurements

A fresh bovine tibia bone was acquired from a local slaughterhouse. A 30-mm disk was extracted from the central shaft region. The disk was further divided into four anatomical quadrants (medial, anterior, lateral, and posterior) using a band saw (EXACT GmbH, Remscheid, Germany).

TABLE II
CORTICAL POROSITY (*Ct.Po*) OBTAINED FROM μCT IN BOVINE BONE PLATES. VALUES ARE MEANS ± STANDARD DEVIATION. WIDTH AND LENGTH OF THE SAMPLES ARE REPORTED IN THE LAST TWO COLUMNS

Sample #	*Ct.Po* (%)	Width (mm)	Length (mm)
1	0.3	23	26
2	0.2	18	28
3	0.9	11	30
4	2.0	12	26

Ex-vivo studies of the human tibia in the elderly found *Ct.Th* in the range between ∼1 and 6 mm [3], [24]. Therefore, parallelepiped plates with variable thickness values in the radial direction (i.e., the direction of sound propagation) were prepared by parallel cuts between periosteal and endosteal interfaces. Length (longitudinal bone direction) and width (circumferential direction) of the samples were then further trimmed. The dimensions of all bovine bone plates are summarized in Tables II and III. Moreover, reference material plates of two polycarbonate (PC), one polyvinylchloride (PVC), three polymethylmethacrylate (PMMA), and four short fiber-reinforced epoxy (Sawbone, Malmoe, Sweden) samples with thickness values between 4 and 8 mm were prepared. The Sawbone samples were prepared such that the fiber orientation was perpendicular to the sound propagation direction. The reference thickness $Ct.Th^{\mathrm{Ref}}$ of each sample was measured by means of a micrometer screw (accuracy: ± 0.002 mm) at five different locations.

C. Reference Measurements

1) Plane Wave Pulse-Echo Ultrasound: The 5-MHz plane wave pulse-echo measurements were conducted using a custom-made scanning acoustic microscope (SAM200 Ex, Q-Bam, Halle, Germany) [25]. The samples were immersed in distilled and degassed water at 37 °C. A custom-made unfocused transducer (diameter = 14.5 mm) was used to scan the samples in two dimensions with a scan increment of 112 μm in both the directions. Center frequency and bandwidth of this transducer were 3.6 MHz and 81%, respectively. The distance between the transducer and the sample surface was in the range between 11 and 17 mm. At each scan position, the pulse-echoes from frontside and backside (FB) reflections of the sample [Fig. 2(a)] were captured at 100 MHz using a 12-b A/D card (Gage Compuscope CS12400, Gage Applied Technologies, Lachine, QC, Canada). Bandpass filtering of the radio frequency (RF) signals was done using a Chebyshev Type II filter in the frequency range from 0.1 to 20 MHz. The time-of-flight difference ΔTOF) between FB reflections was determined using cepstral analysis [9], [11]. In contrast to the commonly used smoothing step necessary to remove the spectral characteristics of the transmit pulse from the oscillations caused by repetitive signals in the power spectrum, we have used the gated front-side reflection of each recorded signal as a reference spectrum [26]. First,

TABLE III

Ct.Th AND $Ct.\nu_{11}$ MEASURED WITH MICROMETER SCREW AND PLANE-WAVE PULSE-ECHO MEASUREMENTS (REF) AND WITH THE MULTIFOCUS METHOD (MF). MEANS, STANDARD DEVIATIONS (SD), AND COEFFICIENTS OF VARIATION (CV) WERE DETERMINED FROM FIVE REPETITIONS

Material		$Ct.Th^{Ref}$ (mm) Mean ± SD	$Ct.Th^{MF}$ (mm) Mean ± SD	CV (%)	$Ct.v_{11}^{Ref}$ (m/s) Mean ± SD	CV (%)	$Ct.v_{11}^{MF}$ (m/s) Mean ± SD	CV (%)
Bovine	#1	1.548 ± 0.005	1.60 ± 0.01	0.3	3318 ± 18	0.5	3301 ± 14	0.4
	#2	2.029 ± 0.003	2.03 ± 0.01	0.4	3304 ± 11	0.4	3312 ± 15	0.5
	#3	2.550 ± 0.010	2.54 ± 0.01	0.3	3290 ± 27	0.8	3246 ± 21	0.6
	#4	4.835 ± 0.034	4.81 ± 0.03	0.5	3319 ± 21	0.6	3309 ± 36	1.1
Sawbone®		1.115 ± 0.005	1.13 ± 0.01	1.0	2830 ± 27	1.0	2844 ± 37	1.3
		1.763 ± 0.007	1.80 ± 0.02	1.0	2988 ± 11	0.4	2935 ± 9	0.3
		2.822 ± 0.002	2.83 ± 0.01	0.2	2866 ± 19	0.7	2803 ± 2	0.1
		4.751 ± 0.004	4.78 ± 0.04	0.7	2970 ± 19	0.6	2932 ± 19	0.7
PMMA		0.906 ± 0.003	0.86 ± 0.01	1.0	2745 ± 8	0.3	2715 ± 5	0.2
		1.946 ± 0.001	1.94 ± 0.01	0.3	2707 ± 2	0.1	2699 ± 3	0.1
		3.908 ± 0.001	4.00 ± 0.01	0.3	2714 ± 1	0.1	2701 ± 4	0.1
PVC		8.160 ± 0.003	8.22 ± 0.03	0.4	2299 ± 1	0.1	2325 ± 3	0.1
Polycarbonate		6.237 ± 0.001	6.24 ± 0.03	0.4	2244 ± 1	0.1	2244 ± 8	0.4
		7.181 ± 0.001	7.15 ± 0.03	0.4	2211 ± 3	0.1	2218 ± 5	0.2

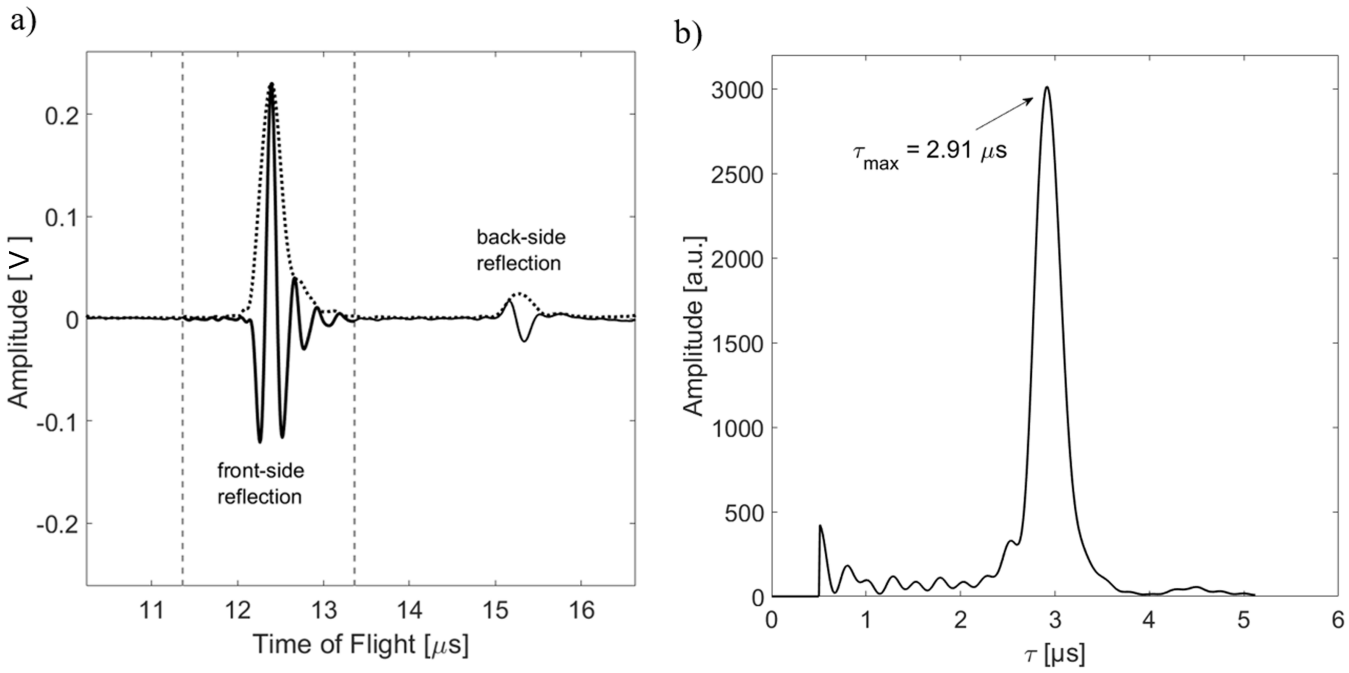

Fig. 2. (a) Pulse-echo signal and Hilbert-transformed envelope signal (black dashed line) from a reference measurement of a 4.84-mm bovine bone plate using an unfocused single-element transducer. A Hanning window (width is indicated by dashed vertical lines) was used to gate the front-side signal. (b) Cepstrum obtained using (1) exhibits a peak at a position that corresponds to the time delay between FB reflections in (a).

the positions of the maxima of FB reflections were determined from the Hilbert-transformed envelope signal using a local peak detection algorithm. Then, Hanning-window gated time segments were created, which extracted either only the front-side reflection (F) or the combined FB signals [Fig. 2(a)]. The power cepstrum $C\tau)$ was obtained from the Fast Fourier Transform (FFT) of the normalized power spectrum

$$C(\tau) = \left|\mathrm{FFT}\left(\log_{10}|S_{\mathrm{FB}}(f)|^2 - \log_{10}|S_F(f)|^2\right)\right| \quad (1)$$

whereas $_{Si}(f)$ is the power spectra of the gated signals F and FB, respectively. Prior to the FFT, the difference spectrum was preconditioned by removing dc and linear components [26] and the calculation was performed within the −6-dB bandwidth of the transducer. The position of the strongest peak in the power cepstrum [Fig. 2(b)] corresponds to ΔTOF. With the thickness values obtained using the micrometer screw, the compressional sound velocity $Ct.v_{11}^{\mathrm{Ref}}$ was obtained

$$Ct.v_{11}^{\mathrm{Ref}} = \frac{2 \cdot Ct.Th^{\mathrm{Ref}}}{\Delta\mathrm{ToF}}. \quad (2)$$

Mean, standard deviation, and coefficient of variation were assessed in homogenous image regions for each sample.

2) Microcomputed Tomography (μCT): High-resolution reference values of $Ct.Th^{\mathrm{Ref}}$ and $Ct.Po^{\mathrm{Ref}}$ of the bovine samples

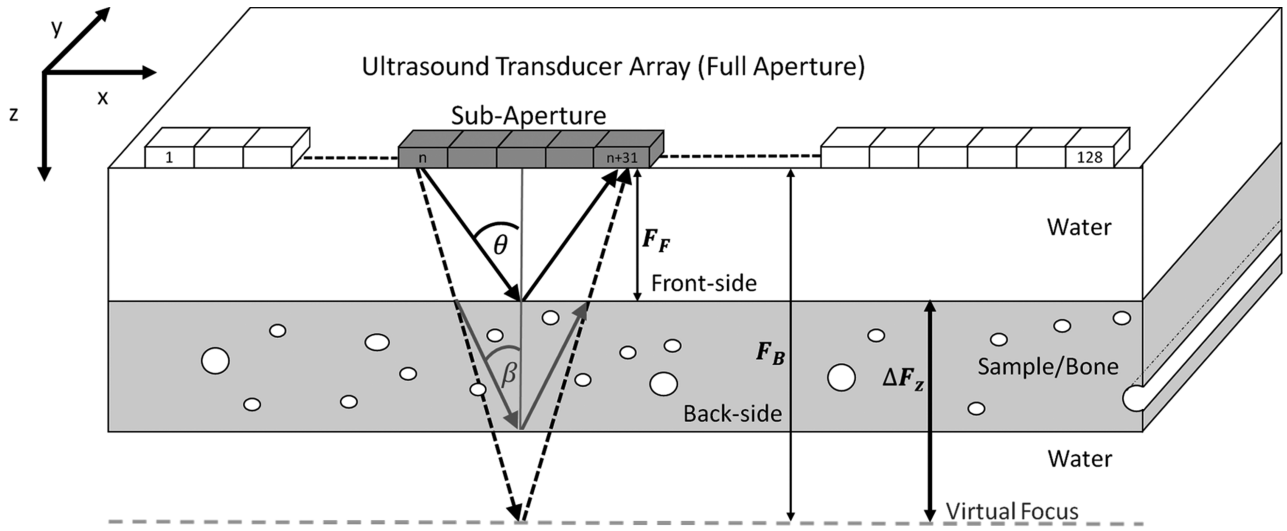

Fig. 3. Schematic illustration of the multifocus measurement in the radial direction (x, z) of a long bone. The transducer is positioned 20 mm above the sample. Focused sound beams are emitted using a 32-element subaperture of a 128-element linear array. The semi-aperture angle θ of the transmit beam is gradually decreased to move the focus from a depth above the sample front side to a position below backside of the sample. Refraction at the front-side interface results in a change the propagation direction of transmitted waves, and thereby, a shift of the focus depth inside the sample. ΔF_Z indicates the shift of the focus depth needed to focus from the frontside (F_F) to the backside (F_B). In addition to the scan of the focus depth, subaperture is scanned along the array (x) direction.

were determined using a SkyScan 1172 scanner (Bruker MicroCT, Kontich, Belgium). The scan parameters were—80 kV; 124 μA; 0.5-mm aluminum filter; exposure time 9.4 s; image averaging over three frames; rotation: 180°; rotation step size: 0.1°; and field of view: 8 × 8 mm^2. The image reconstruction was performed using the NRecon reconstruction software (v.1.10.1, Skyscan NV, Kontich, Belgium) with the following settings—beam hardening correction: 25%; ring artifact reduction: 45; and manual postalignments depending on the samples. The isotropic voxel size of the reconstructed volume data was 11.94 μm. For each examination, a stack of 1.246 cross-sectional images was stored in 8-b file format. A 3-D Gaussian smoothing kernel with standard deviation of 1.2 and a 2-D median filter with a size of 50 × 50 was applied to remove noise from the images. Pores and bone matrix were segmented using Otsu's method [27]. A rectangular volume of interest (VOI) with margins 0.2 mm inside the sample limits was manually defined. Within each VOI, the porosity $Ct.Po^{\mathrm{Ref}}$ was determined by the ratio between pore voxels and total number of voxels within the VOI. The error of the porosity estimation with this setup is in the order of $< 0.2\%$ [28].

D. Multifocus Ultrasound Acquisition

Multifocus imaging was performed with a medical ultrasound scanner SonixTOUCH equipped with a 3-D linear array transducer 4DL14-5/38 (consisting of a 1-D 128-element array, center frequency 8 MHz, pitch 0.3 mm, and a sweep motor that allows automatic acquisition of 3-D volumes), and a SonixDAQ single-channel data acquisition system (Ultrasonix, Richmond, BC, Canada). The SonixDAQ is a research add-on that allows simultaneous pre-beamformed single-channel RF data acquisition of all 128 channels. The samples were immersed and degassed in water for 30 min. Fig. 3 shows the multifocus setup. The transducer array was positioned perpendicular to the bone long axis and parallel to the bone surface. The measurement sequence consisted of a series of conventional B-mode imaging sequences with $N_{\mathrm{Tx}} = 128$ lateral scan positions x_i. At each x_i scan position, sound waves were focused on the radial bone direction into the plates using a 32-element transmit aperture. Subsequent B-mode images were acquired with gradually increasing focus depths F_z (16 steps; starting from 10 mm with a step size of 2 mm). The semi-aperture angle θ was defined by aperture size and focus depth F_z. In order to optimize penetration depth, the transducer elements were not excited at their resonance frequency, but with a single "+" signal at a system transmit frequency of 5 MHz, which produced signals with a center frequency of 5.1 MHz and a bandwidth of 69% [Fig. 4(d)]. Single-channel RF data ($N_{\mathrm{Rx}} = 128$) were captured at a sampling rate of 40 MHz with 12-b resolution, resulting in a 4-D Matrix $V(N_{\mathrm{Tx}}, F_z, N_{\mathrm{Rx}}, t)$ with dimensions 128 × 16 × 128 × 1023. The temperature of the water was measured during the acquisition throughout to calculate sound velocities in water v_{H20} depending on temperature following [29]. All measurements were repeated five times with sample repositioning between measurements.

E. Image and Signal Processing

Beamformed images were reconstructed using the same aperture and focus depth as for the transmit beams, resulting in a 3-D matrix $V_{\mathrm{Rx-focus}}(F_z, x, t)$. For visualization of the confocal reflection amplitudes, a maximum projection image $V_{\mathrm{MPI}}(x, t)$ was created [Fig. 4(a)]. The time of flights [$\mathrm{TOF}_F(x, z)$ and $\mathrm{TOF}_B(x, z)$] and amplitudes [$V_F(x, F_z)$ and $V_B(x, F_z)$] of reflections from the sample's FB, respectively, were tracked for each array scan position and focus depth

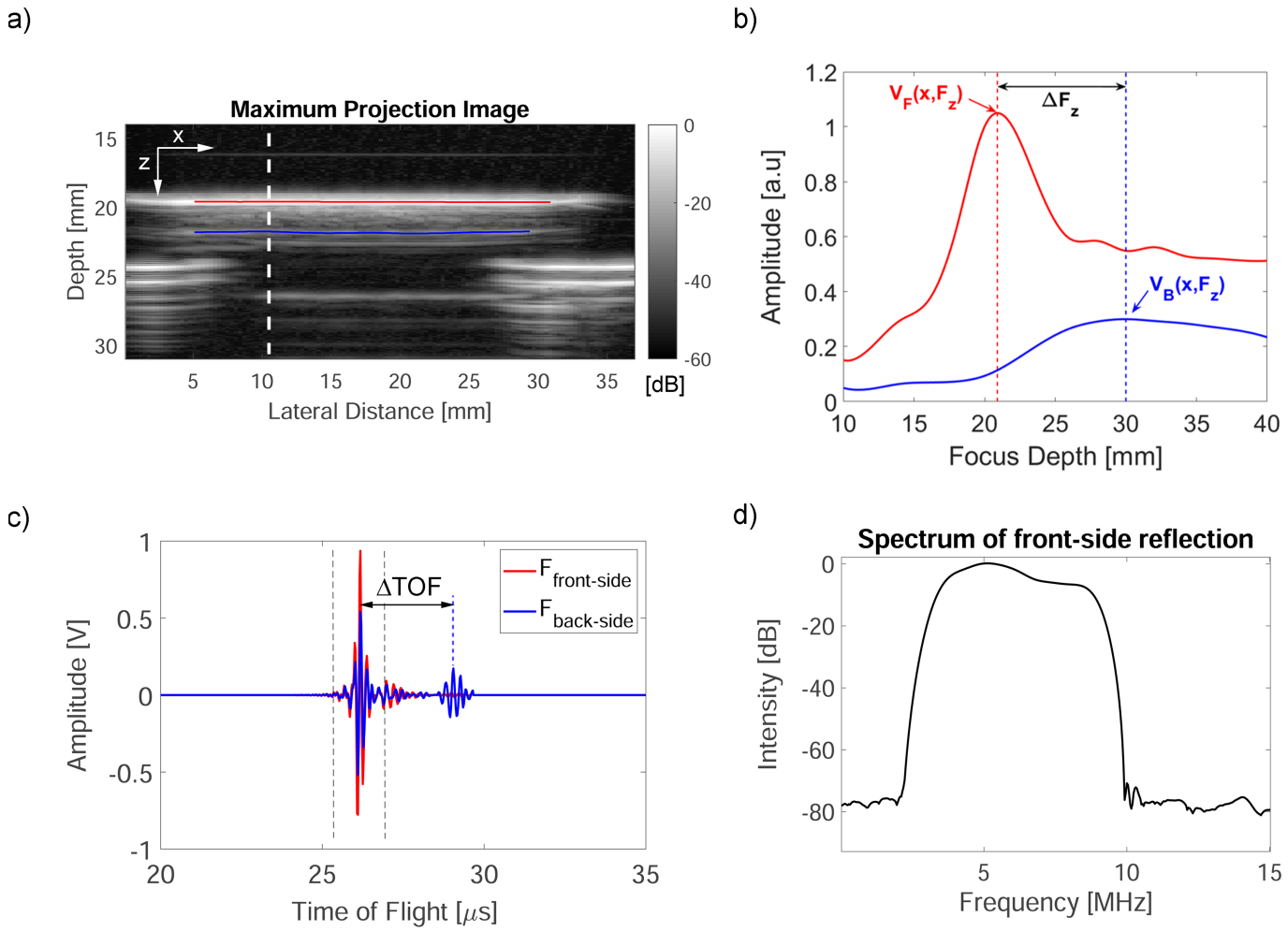

Fig. 4. (a) Maximum projection B-mode image reconstructed from all focus depths with tracked front (red line) and backside surfaces (blue line) of a bovine sample. (b) Tracked amplitudes at the lateral scan position indicated by a white dashed line in (a) of front (red line) and backside surface reflections (blue line) of a 4.79-mm bovine sample versus focus depth. The confocal FB focus positions can be determined from the maxima of $V_F(x, F_Z)$ and $V_B(x, F_Z)$. (c) Corresponding beamformed pulse-echo signals with confocal beamforming at 21 mm ($F_{\text{frontside}}$) and 30 mm (F_{backside}). The vertical dashed lines indicate the time gate for the calculation of the power spectrum. (d) Mean power spectrum of all gated front-side echoes.

[Fig. 4(b)] and the ΔTOF between confocal frontside and backside reflections was determined.

For each lateral scan position x_i, the $\Delta\text{TOF}(x_i)$ between confocal FB reflections and the focus shift ΔF_z between confocal FB positions were determined [Fig. 4(c)]. The shift ΔF_z needed to focus from the front to the backside is determined by the sample thickness $Ct.Th$, the semi-aperture angle θ of transmit and receive beams, and the sound velocities in water v_{H20} and bone $Ct.v_{11}$ [30], [31]

$$Ct.Th = \frac{\Delta F_z}{0.5\frac{Ct.v_{11}}{v_{H_2O}} \cdot \left(1 - \frac{Ct.v_{11}^2}{v_{H_2O}^2}\right) \cdot (1 - \cos(k_{\text{eff}}\theta)) - \frac{Ct.v_{11}}{v_{H_2O}}}. \tag{3}$$

The factor k_{eff} in (3) accounts for: 1) the increasing conversion of compressional waves into shear waves with increasing angle of incidence and 2) the complete lack of compressional wave transmission into the solid for inclination angles larger than a critical angle θ_{crit}

$$\theta_{\text{crit}} = \arcsin\left(\frac{v_{H_2O}}{Ct.v_{11}}\right). \tag{4}$$

$k_{\text{eff}}\theta$ can be interpreted as an effective aperture contributing to the beam focusing on the backside. The factor k_{eff} depends on the semi-aperture θ and the transmittance and reflectance functions. In this study, an algorithm was developed to estimate k_{eff} based on θ and θ_{crit} and k_{eff} was derived for each measurement iteratively.

The scanning of the beams along the array (x_i) direction enables local estimations of sound velocity and thickness. The lateral resolution of the estimates is determined by the lateral beamwidth interrogating the sample while focusing on the backside of the sample. Therefore, $Ct.v_{11}(x_i)$ and $Ct.Th(x_i)$ estimations were smoothed using a robust moving average filter with a span of 21 prior to the calculations of sample means and standard deviations.

F. Statistics

The normality of the parameter distributions was confirmed using the Lilliefors test. Pearson linear regression analysis and Bland–Altman plots [32] were conducted to compare the parameters obtained using the multifocus method with reference values. Precision was defined as the coefficient of

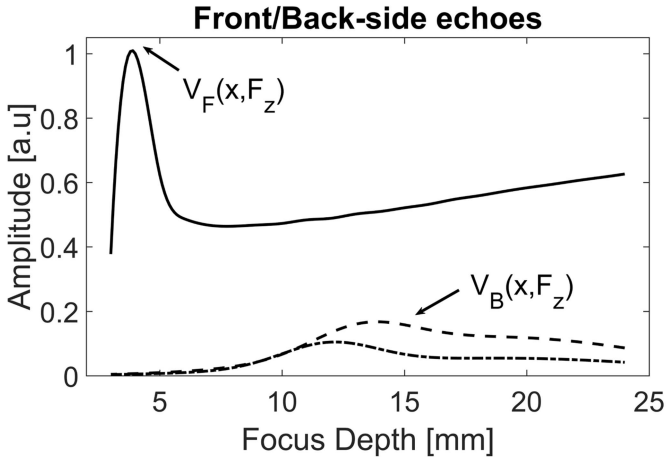

Fig. 5. Representative result of the tracking of front (black line) and backside reflections (–: $Po = 0\%$; - ·: $Po = 13\%$) using the multifocus approach.

variation (CV) of the difference between predicted and reference relative to the mean of the reference values. Accuracy was determined by means of the root-mean-squared error compared with the reference values. Reproducibility was assessed as the intrasample CV of repeated measurements. If parameters were normally distributed, paired t-tests were used to evaluate if the parameters estimated using the multifocus method were significantly different compared with the reference methods. Otherwise a Wilcoxon rank-sum test was used. The significance level was defined as $p < 0.05$. All analyses were performed using the MATLAB including the Signal Processing, Curve Fitting, and Statistics Toolboxes (The Mathworks, Natick, MA, USA).

III. Results

A. Numerical Simulations

The FB echo amplitudes and their corresponding TOF could be retrieved from all simulation models. A representative result of the tracking of FB reflections is shown in Fig. 5.

For all simulations, the peak of the surface echo occurred at a focus depth of 4 mm. In contrast, the peak position and amplitude of the backside reflection varied depending on the pore properties. For a homogenous bone plate with 0% porosity, the confocal backside position was at a focus depth of 14 mm. All models which contained pores exhibited decreased confocal backside amplitudes and focus depth positions.

The simulation results of model I revealed a dependence of the estimated sound velocity ($Ct.v_{11}^{\mathrm{MF}}$) on the reference velocity ($Ct.v_{11}^{\mathrm{Ref}}$) if the semi-aperture θ was close to the critical angle. The following algorithm was applied to all subsequent analyses:

$$k_{\mathrm{eff}} = \begin{pmatrix} 1 \text{ if } \theta < \theta_{\mathrm{crit}} - 10^{\circ} \\ 0.1 \cdot \Delta\theta \text{ if } \theta > \theta_{\mathrm{crit}} - 10^{\circ} \end{pmatrix} \tag{5}$$

whereas $\Delta\theta = \theta_{\mathrm{crit}} - \theta$. The factor k_{eff} was determined in five iterations, starting with $k_{\mathrm{eff}} = 1$.

All parameters obtained from model I ($Ct.Po.Dm = 40\ \mu$m) were normally distributed. $Ct.v_{11}$ decreased with increasing sample porosity [Fig. 6(a)]. The accuracy and precision of the multifocus method were 36.9 m/s and 1.1%, respectively [Fig. 6(b)]. The $Ct.v_{11}^{\mathrm{MF}}$ values were not significantly different from the reference values $Ct.v_{11}^{\mathrm{Ref}}$. Accuracy and precision of the estimation of $Ct.Th^{\mathrm{MF}}$ were 0.04 mm and 1.0%, respectively [Fig. 6(c)]. The estimations were not significantly different from the model thickness.

Except for the reference velocity values, all parameters obtained from model II ($Ct.Po = 10\%$) were normally distributed. $Ct.v_{11}$ decreased with a decreasing pore size (or increasing pore density) [Fig. 7(a)]. The $Ct.v_{11}^{\mathrm{MF}}$ values were not significantly different from the values obtained from reference method [Fig. 7(b)]. The accuracy and precision of the multifocus method were 52 m/s and 1.8%, respectively. Cortical thickness estimations $Ct.Th^{\mathrm{MF}}$ were not significantly different from the model thickness. Accuracy and precision were 0.26 mm and 6.3%, respectively [Fig. 7(c)]. It should be noted that both accuracy and precision decreased for very large-pore diameters.

B. Multifocus Measurements

The multifocus method failed on the first and last array scan positions, for which only a part of the 32-channel aperture could be used for beamforming. However, FB echo amplitudes and their corresponding TOF could be retrieved from all samples for at least 40 out of the 128 beamformed scan positions. Cortical thickness and porosity values of the bovine samples are summarized in Table II. Table III contains parameters obtained from reference and multifocus methods for each sample. The reproducibility of $Ct.v_{11}^{\mathrm{MF}}$ and $Ct.Th^{\mathrm{MF}}$ were 0.52% and 0.44%, respectively.

For the nonporous polymer samples, no variations of $Ct.Th^{\mathrm{MF}}$ and $Ct.v_{11}^{\mathrm{MF}}$ with respect to the array position were observed [Fig. 8(a)]. A higher variability along the scan position was observed in the bovine samples, particularly in that with the highest porosity of 2% (Table II). It should be noted that pronounced local variations occurred for $Ct.v_{11}^{\mathrm{MF}}$ but not for $Ct.Th^{\mathrm{MF}}$ [Fig. 8(b)].

All derived mean parameters were normally distributed. The $Ct.v_{11}$ and $Ct.Th$ values obtained from the multifocus method were not significantly different from the values obtained using the reference methods (Fig. 8). Accuracy and precision were 24.1 m/s and 0.89%, respectively, for $Ct.v_{11}^{\mathrm{MF}}$ and 0.04 mm and 1.13%, respectively, for $Ct.Th^{\mathrm{MF}}$ (Fig. 9).

IV. Discussion

This study describes a simple method that allows the simultaneous estimation of thickness and compressional sound velocity in plate-shaped cortical bone samples using a phased-array ultrasound. The method uses refraction occurring at the interface between the soft and hard materials and refraction-corrected focusing to provide a multifocus image of both interfaces of the plate. We applied confocal transmit and receive beamforming, peak detection, and signal tracking algorithms, and an iterative approximation of an effective aperture to retrieve $Ct.v_{11}^{\mathrm{MF}}$ and $Ct.Th^{\mathrm{MF}}$. A parametric numerical

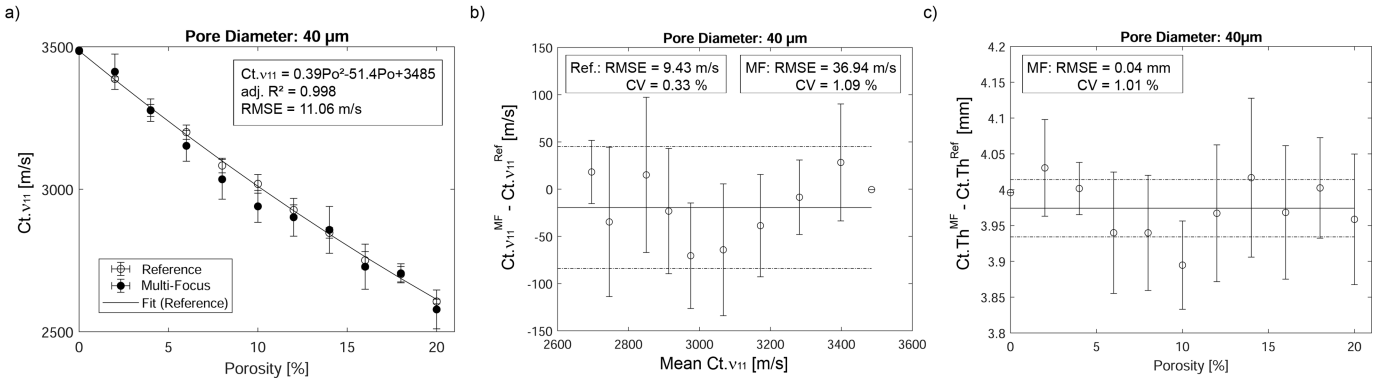

Fig. 6. Estimation of SOS and thickness in model I (pore size: 40 μm, variable pore density). (a) Sound velocity decreased with increasing porosity (white dots: reference method and black dots: multifocus method). (b) Bland–Altman plot of $Ct.\nu_{11}^{MF}$ versus $Ct.\nu_{11}^{Ref}$. (c) Difference between $Ct.Th^{MF}$ and model thickness ($Ct.Th^{Ref} = 4$ mm) as a function of porosity. The mean differences [horizontal straight lines in (b) and (c)] were not significantly different from the reference values.

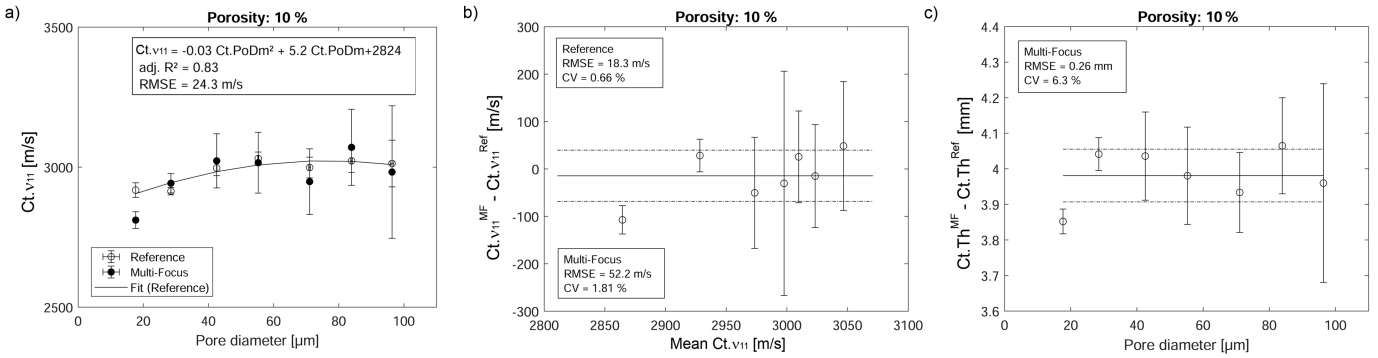

Fig. 7. Estimation of SOS and thickness in model II (porosity: 10%, variable pore size). (a) Sound velocity decreased for small pore sizes ($Ct.Po.Dm < 40$ μm) was smaller than the values for larger pores (white dots: reference method and black dots: multifocus method). (b) Bland–Altman plot of $Ct.\nu_{11}^{MF}$ versus $Ct.\nu_{11}^{Ref}$. (c) Difference between $Ct.Th^{MF}$ and model thickness ($Ct.Th^{Ref} = 4$ mm) as a function of porosity. The mean differences [horizontal straight lines in (b) and (c)] were not significantly different from the reference values.

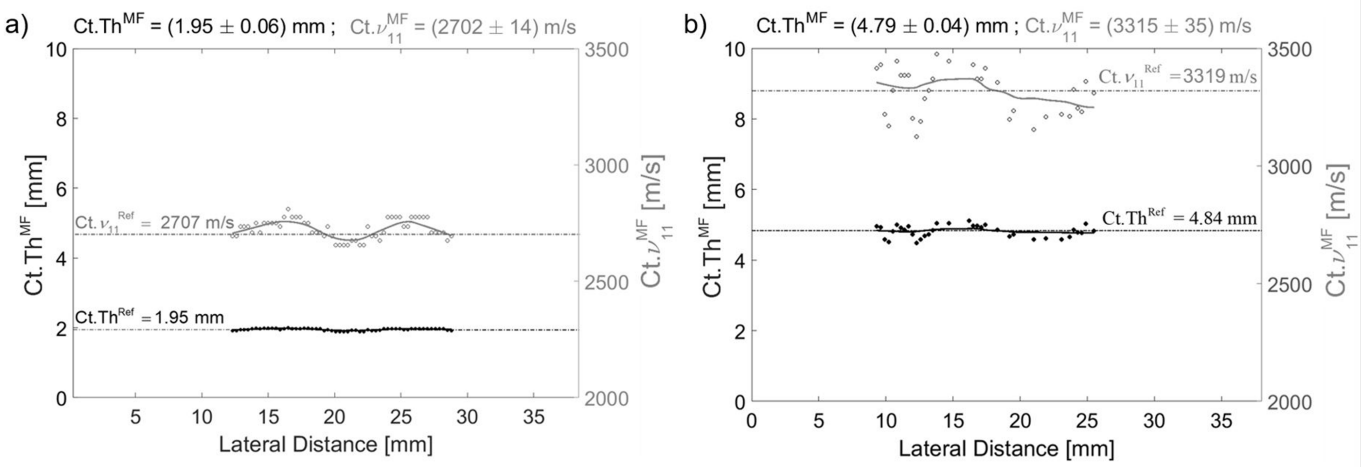

Fig. 8. Representative plots of $Ct.Th^{MF}(x_i)$ and $Ct.\nu_{11}^{MF}(x_i)$ obtained from (a) PMMA plate and (b) bovine bone plate. The dots indicate the estimations for each individual array position, and the straight lines are the estimations using a moving average filter. Means and standard deviations were determined from the smoothed data. The number of individual scan positions contributing to the parameter estimations in (a) and (b) were 56 and 40, respectively.

simulation study was conducted to test the method on idealized porous structures with randomlydistributed pores of variable size and density. Reproducibility, accuracy, and precision of the method were assessed experimentally on homogenous and heterogeneous polymer phantoms and on bovine cortical bone plates.

A. Numerical Simulations

The ability to apply the method for a typical cortical bone pore size and variable pore densities resulting in porosities up to 20% was shown in model I. The observed decrease of $Ct.\nu_{11}$ with increasing porosity is consistent with the

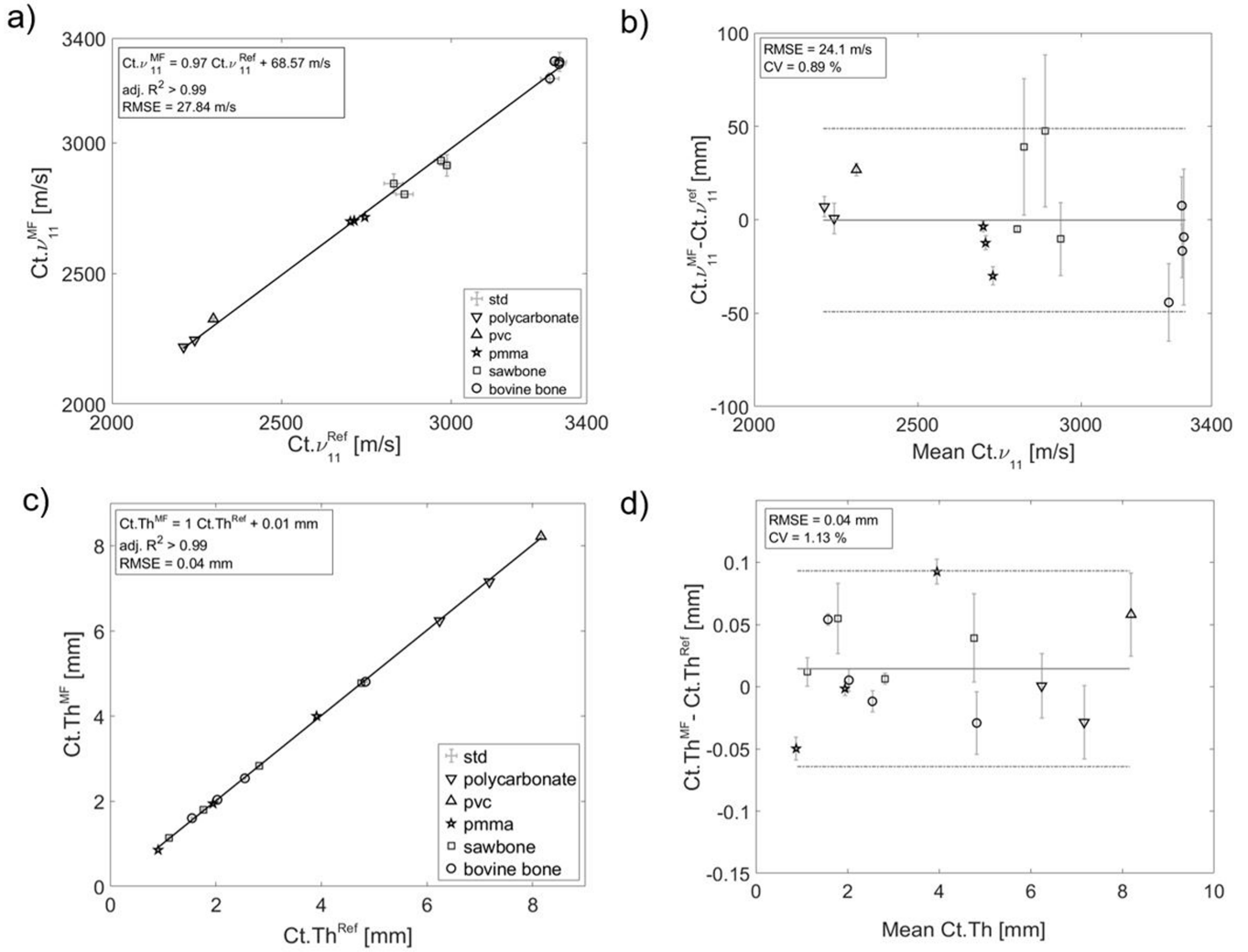

Fig. 9. Experimentally derived $Ct.\nu_{11}$ (a) and (b), and $Ct.Th$ (c) and (d). The mean differences [horizontal straight lines in (c) and (d)] were not significantly different from the reference values.

well-established assumption that elastic properties of cortical bone can be approximated by a two-phase model consisting of a solid extracellular matrix pervaded by fluid-filled pores with a certain pore volume fraction [33]. To compare their values with our data, we calculate the compound mass density using the upper bound rule of mixtures for composites, i.e., $Ct.\rho_{\text{Compound}} = Ct.Po \cdot \rho_{H_2O} + (1 - Ct.Po) \cdot \rho_{\text{Tissue}}$, whereas ρ_{Tissue} is the density of the bone tissue matrix (Table I). The elastic stiffness coefficients at 0% and 20 % porosity are obtained from $Ct.c_{11}(Ct.Po) = \rho_{\text{Compound}}(Ct.Po) \cdot (Ct.\nu_{11}(Ct.Po))^2$. The relative decrease of the elastic coefficient $Ct.c_{11}$ of approximately 38.4% for an increase in $Ct.Po$ from 0% to 20 % reported in [33] was considerably smaller than the decrease of $Ct.c_{11}$ of 59% obtained in our study. The larger decrease with increasing porosity observed in our model suggests that pore density has an impact on $Ct.\nu_{11}$ in addition to porosity. This was also apparent in model II, in which porosity was kept constant. For increasing pore densities realized by a decrease of the pore size, a gradual decrease of $Ct.\nu_{11}$ was observed [Fig. 7(a)]. The resulting variations of $Ct.\nu_{11}$ and $Ct.c_{11}$ in the evaluated pore size range were 2.8% and 5.5%, respectively. A possible explanation is that an increase of pore density increases the number of multiple scatter events, and thereby, also increases the effective propagation path length, which is in agreement with recent studies of Yousefian *et al.* [34] and Karbalaeisadegh *et al.* [35], who investigated the effects of pore size and density on ultrasound attenuation in similar models. It should also be noted that models with very large-pore sizes and low pore densities resulted in high variability of the parameter estimates, both for the reference and the multifocus methods. This is reasonable, as, in these models, the assumption of a random pore distribution was not fulfilled anymore. In summary, the strong dependence of sound velocity in the radial direction on porosity confirms: 1) the necessity to assess this parameter in order to quantify cortical thickness; 2) that a change in $Ct.\nu_{11}$ is a good surrogate parameter for changes in cortical porosity. However, the effects of variable matrix stiffness caused by age [36] or pathologies [37] and the pore architecture on the association between $Ct.\nu_{11}$ and $Ct.Po$ need to be considered.

B. Multifocus Measurements

The experiments using a 128-element linear phased array probe was performed on nonporous, homogeneous plates

(PMMA, PC, and PVC), on a heterogenous Sawbone composite polymer, and on bovine plates with low porosity. The elements were excited with a frequency of 5 MHz to ensure a good combination of penetration depth and temporal resolution. The evaluated samples provided a range of sound velocities and thickness values typically found in human cortical bone. The sound velocity values measured in Sawbone ($Ct.v_{11}^{\mathrm{MF}} = 2883 \pm 57$ m/s) were consistent with our reference measurements and with values reported by others [12], [14]. In the porous bone samples, the variability of $Ct.v_{11}^{\mathrm{MF}}$ along the probe was higher compared with that in the polymer plates (Fig. 9). As the plate thickness was invariant within a sample, it demonstrates the ability of the method to resolve and visualize local variations of $Ct.v_{11}$.

Accuracy and precision observed in the experiments were considerably better than those observed in the simulations. This is not surprising, since *in-silico* estimations of *Ct.Th* and $Ct.v_{11}$ consisted of six individual model realizations, while the experiments consisted of at least 40 estimations per measurement and five repetitions.

Wydra *et al.* [38] have used a similar refraction measurement approach and reported for measurements on porous plate-shaped skull bone phantoms precision values of 8.5% and 4.1% for thickness and SOS, respectively. Their precision values in pore-free phantoms were approximately 50% lower. In contrast, our experimental precision values were much better ($< 1.5\%$ for SOS and thickness), which can be attributed to both the higher frequency (5 versus 2.25 MHz) and the consideration of an effective aperture in our study. An *ex-vivo* accuracy of 0.2 mm of the thickness estimation in human radius bones using 0.5-MHz guided waves in axial transmission at human has been reported by Schneider *et al.* [24]. Although the accuracy of 0.03 mm of the multifocus was considerably better, the different samples' geometries (plates versus real irregular periosteal and endosteal bone boundaries) prohibit a direct comparison. Future studies should, therefore, assess the performance of the multifocus method on real human cortical bones.

However, a fundamental advantage of the proposed method in comparison with the guided-wave method is that it provides direct image guidance. The bone surface is clearly visible in the ultrasound image allowing optimal probe positioning prior to the data acquisition. Although it was not implemented in the current study, multifocus beamforming, reconstruction of the maximum projection image, and interface tracking could, in principle, be performed in real time. Thereby, the operator would have immediate visual feedback about the measurement success and high failure rates, e.g., up to 20% for axial transmission measurements [16], [39] could be avoided. This was not possible with the used system, as the time for the transfer of data from the data acquisition box to the hard drive (27 s), data conversion (42 s), and beamforming on standard CPU (61 s) was too long, but could be achieved with GPU-based ultrafast imaging platforms.

Another approach to measure the cortical bone thickness and SOS using refraction-corrected imaging with a 2.5-MHz linear phased array transducer has been proposed by Renaud *et al.* [18]. In contrast to the multifocus method, they use single-element excitation, full-array waveform capture, and an ultrasound image reconstruction adapted from seismology, which also provides information about elastic anisotropy. The concept of finding the optimal focus quality by incorporating variable sound velocities along the propagation paths for the delay-and-sum image reconstruction is similar to our approach. Key differences of the multifocus approach are that: 1) transmission losses caused by refraction and mode conversion at the periosteal bone interface are considered to obtain correct thickness and velocity values and 2) 32-element focused beams are used instead beams emitted from single elements. The latter may result in a smaller signal-to-noise ratio compared with multi-element transmit and receive focusing, which should be elaborated in future studies.

C. Limitations

Our study has several limitations. Both the numerical and experimental studies were restricted to simple plate-shaped geometries. The cortical microstructure bone was simulated using randomly distributed circular pores of uniform size. The parameter estimation relies on the estimations of ΔTOF and ΔF_z. In particular, the confocal peak arising from the backside reflection was less sharp compared with that from the front side. The sharpness of the backside peak depends on many factors, e.g., frequency, bandwidth, signal-to-noise ratio, aperture angle, critical angle, plate thickness, porosity, flatness, and roughness of FB interfaces. Curved and irregular bone interfaces [38] and heterogenous pore sizes with pore size gradients, typically found in human cortical bones, particularly in osteoporotic bones, will lead to additional phase distortions of the propagating wave. While a comprehensive analysis of individual effects on the accuracy of the estimations ΔTOF and ΔF_z was beyond the scope of this study and the incorporation of appropriate phase aberration correction algorithms was not necessary for the current study, these aspects should be considered in the future based on more the realistic simulation models. Moreover, future experimental studies should target human bone instead of the bovine plexiform bone used in this study to demonstrate the applicability of the method also for the clinically relevant tissue types with higher porosities. Another limitation of our simulation model was the frequency-independent absorption. Although the major contribution of frequency-dependent attenuation can be considered to arise from the scattering on pores rather than from absorption [34], other simulation codes may be better suited to investigate their relative impacts.

D. Transition to In Vivo Measurements

This study demonstrates the assessment of *Ct.Th* and $Ct.v_{11}$ *ex vivo* using a clinical ultrasound scanner. To approve the *in vivo* feasibility of the multifocus imaging technique, the implementation of the aforementioned phase-aberration corrections, more sophisticated algorithms for the detection of the bone surface, eventually in combination with edge-enhancing image filters are required. Moreover, the method can only be applied with the imaging plane

parallel to the plane of transverse isotropy, i.e., the radial direction perpendicular to the long bone axes [40]. Potential measurement regions are shaft regions, in which the cortical thickness is not much smaller than 1 mm, and the geometry is approximately plate-shaped, e.g., the medial portion of the tibia. However, the application to other large long bones, such as radius or femur, or to smaller bones, such as phalanges or jawbones, is also feasible. For the latter, probes with higher frequencies and smaller form factors should be used.

E. Clinical Use of Ultrasound Parameters

The developed technique is anticipated to have high clinical potential since it uses conventional medical ultrasound technology, is noninvasive and nonionizing and can assess locally *Ct.Th* and $Ct.v_{11}$ with image guidance at multiple skeletal sites. Previous studies have already demonstrated the high relevance of cortical SOS [41]–[43] and thickness [24], [39] measured by axial transmission as biomarkers for bone quality. Cortical bone of the tibia has been proposed as a favorable measurement site for the prediction of bone fracture risk since it is load bearing, can be easily measured by ultrasound, and changes in thickness and pore morphology, i.e., the prevalence of large pores are associated with a mechanical impairment of the hip [3]. Moreover, a recent *in vivo* study by Minonzio *et al.* [16] has demonstrated that *Ct.Th* and *Ct.Po* derived from full-wave dispersion axial transmission at the distal radius in postmenopausal women are suitable biomarkers for the discrimination of nontraumatic fracture from nonfractured cases and that distinct associations of the two biomarkers with fracture location exist, even in cases in which fractures were not associated with any DXA-based parameter. Compared with axial transmission methods, no dedicated hardware is required for the multifocus measurement, and the parameter estimations are locally resolved within the imaging plane and provide image guidance. Therefore, it has a high potential as an add-on or even alternative to X-ray imaging, particularly for longitudinal and pediatric applications. The implementation of *Ct.Th* and $Ct.v_{11}$ as complementary diagnostic biomarkers may improve fracture risk prediction.

V. Conclusion

This work shows that cortical thickness and the compressional sound velocity in the radial direction can be determined precisely using refraction-corrected multifocus imaging. The method was developed and tested *in-silico* and experimentally on plate-shaped polymer samples, cortical bone phantoms, and on bovine tibia bone samples. For reliable parameter estimation, refraction and wave conversion losses at the bone surface must be considered. The derived parameters showed excellent agreement with reference values.

VI. Conflicts of Interest

Dr. J. Du and Dr. K. Raum have the patent "CortBS: Ultrasonic method for determining pore dimensions in cortical bone" pending.

References

[1] E. Hernlund *et al.*, "Osteoporosis in the European Union: Medical management, epidemiology and economic burden: A report prepared in collaboration with the international osteoporosis foundation (IOF) and the European federation of pharmaceutical industry associations (EFPIA)," *Arch. Osteoporosis*, vol. 8, p. 136, Dec. 2013.

[2] R. Zebaze and E. Seeman, "Cortical bone: A challenging geography," *J. Bone Mineral Res.*, vol. 30, no. 1, pp. 24–29, 2015.

[3] G. Iori *et al.*, "Large cortical bone pores in the tibia are associated with proximal femur strength," *PLoS ONE*, vol. 14, no. 7, 2019, Art. no. e0215405.

[4] K. K. Nishiyama, H. M. Macdonald, H. R. Buie, D. A. Hanley, and S. K. Boyd, "Postmenopausal women with osteopenia have higher cortical porosity and thinner cortices at the distal radius and tibia than women with normal aBMD: An *in vivo* HR-pQCT study," *J. Bone Mineral Res.*, vol. 25, no. 4, pp. 882–890, 2010.

[5] E. S. Siris *et al.*, "Bone mineral density thresholds for pharmacological intervention to prevent fractures," *Arch. Internal Med.*, vol. 164, no. 10, pp. 1108–1112, 2004.

[6] S. C. E. Schuit *et al.*, "Fracture incidence and association with bone mineral density in elderly men and women: The Rotterdam study," *Bone*, vol. 34, no. 1, pp. 195–202, 2004.

[7] S. A. Wainwright *et al.*, "Hip fracture in women without osteoporosis," *J. Clin. Endocrinol. Metabolism*, vol. 90, no. 5, pp. 2787–2793, 2005.

[8] P. H. F. Nicholson, "Ultrasound and the biomechanical competence of bone," *IEEE Trans. Ultrason., Ferroelectr., Freq. Control*, vol. 55, no. 7, pp. 1539–1545, Jul. 2008.

[9] J. Karjalainen, O. Riekkinen, J. Toyras, H. Kroger, and J. Jurvelin, "Ultrasonic assessment of cortical bone thickness *in vitro* and *in vivo*," *IEEE Trans. Ultrason., Ferroelectr., Freq. Control*, vol. 55, no. 10, pp. 2191–2197, Oct. 2008.

[10] J. P. Karjalainen *et al.*, "Multi-site bone ultrasound measurements in elderly women with and without previous hip fractures," *Osteoporosis Int.*, vol. 23, no. 4, pp. 1287–1295, 2012.

[11] K. A. Wear, "Autocorrelation and cepstral methods for measurement of tibial cortical thickness," *IEEE Trans. Ultrason., Ferroelectr., Freq. Control*, vol. 50, no. 6, pp. 655–660, Jun. 2003.

[12] Y. Tasinkevych, J. Podhajecki, K. Falińska, and J. Litniewski, "Simultaneous estimation of cortical bone thickness and acoustic wave velocity using a multivariable optimization approach: Bone phantom and *in-vitro* study," *Ultrasonics*, vol. 65, pp. 105–112, Feb. 2016.

[13] R. Zheng, L. H. Le, M. D. Sacchi, and E. Lou, "Imaging internal structure of long bones using wave scattering theory," *Ultrasound Med. Biol.*, vol. 41, no. 11, pp. 2955–2965, 2015.

[14] J. Foiret, J.-G. Minonzio, C. Chappard, M. Talmant, and P. Laugier, "Combined estimation of thickness and velocities using ultrasound guided waves: A pioneering study on *in vitro* cortical bone samples," *IEEE Trans. Ultrason., Ferroelectr., Freq. Control*, vol. 61, no. 9, pp. 1478–1488, Sep. 2014.

[15] M. Granke, Q. Grimal, A. Saïed, P. Nauleau, F. Peyrin, and P. Laugier, "Change in porosity is the major determinant of the variation of cortical bone elasticity at the millimeter scale in aged women," *Bone*, vol. 49, no. 5, pp. 1020–1026, 2011.

[16] J.-G. Minonzio *et al.*, "Ultrasound-based estimates of cortical bone thickness and porosity are associated with nontraumatic fractures in postmenopausal women: A pilot study," *J. Bone Mineral Res.*, vol. 34, no. 9, pp. 1585–1596, 2019.

[17] P. Moilanen *et al.*, "Modeling the impact of soft tissue on axial transmission measurements of ultrasonic guided waves in human radius," *J. Acoust. Soc. Amer.*, vol. 124, no. 4, pp. 2364–2373, 2008.

[18] G. Renaud, P. Kruizinga, D. Cassereau, and P. Laugier, "*In vivo* ultrasound imaging of the bone cortex," *Phys. Med. Biol.*, vol. 63, no. 12, 2018, Art. no. 125010.

[19] E. Bossy, M. Talmant, and P. Laugier, "Three-dimensional simulations of ultrasonic axial transmission velocity measurement on cortical bone models," *J. Acoust. Soc. Amer.*, vol. 115, no. 5, pp. 2314–2324, 2004.

[20] D. Rohrbach *et al.*, "Spatial distribution of tissue level properties in a human femoral cortical bone," *J. Biomech.*, vol. 45, no. 13, pp. 2264–2270, 2012.

[21] M. Sasso, G. Haïat, Y. Yamato, S. Naili, and M. Matsukawa, "Frequency dependence of ultrasonic attenuation in bovine cortical bone: An *in vitro* study," *Ultrasound Med. Biol.*, vol. 33, no. 12, pp. 1933–1942, 2007.

[22] C. Chappard *et al.*, "3D characterization of pores in the cortical bone of human femur in the elderly at different locations as determined by synchrotron micro-computed tomography images," *Osteoporosis Int.*, vol. 24, no. 3, pp. 1023–1033, 2013.
[23] L. P. Bakalova *et al.*, "Intracortical bone mechanics are related to pore morphology and remodeling in human bone," (in English), *J. Bone Mineral Res.*, vol. 33, no. 12, pp. 2177–2185, 2018.
[24] J. Schneider *et al.*, "*Ex vivo* cortical porosity and thickness predictions at the tibia using full-spectrum ultrasonic guided-wave analysis," *Arch. Osteoporosis*, vol. 14, no. 1, p. 21, 2019.
[25] S. Lakshmanan, A. Bodi, and K. Raum, "Assessment of anisotropic tissue elasticity of cortical bone from high-resolution, angular acoustic measurements," *IEEE Trans. Ultrason., Ferroelectr., Freq. Control*, vol. 54, no. 8, pp. 1560–1570, Aug. 2007.
[26] S. Lakshmanan *et al.*, "Prediction of the intramuscular fat content in loin muscle of pig carcasses by quantitative time-resolved ultrasound," *Meat Sci.*, vol. 90, no. 1, pp. 216–225, 2012.
[27] N. Otsu, "A threshold selection method from gray-level histograms," *IEEE Trans. Syst., Man, Cybern.*, vol. 9, no. 1, pp. 62–66, Jan. 1979.
[28] H. M. Britz, J. Jokihaara, O. V. Leppänen, T. Järvinen, and D. M. L. Cooper, "3D visualization and quantification of rat cortical bone porosity using a desktop micro-CT system: A case study in the tibia," *J. Microsc.*, vol. 240, no. 1, pp. 32–37, 2010.
[29] W. Marczak, "Water as a standard in the measurements of speed of sound in liquids," *J. Acoust. Soc. Amer.*, vol. 102, no. 5, pp. 2776–2779, Nov. 1997.
[30] K. I. Maslov, L. M. Dorozhkin, V. S. Doroshenko, and R. G. Maev, "A new focusing ultrasonic transducer and two foci acoustic lens for acoustic microscopy," *IEEE Trans. Ultrason., Ferroelectr., Freq. Control*, vol. 44, no. 2, pp. 380–385, Mar. 1997.
[31] K. Raum and J. Brandt, "Simultaneous determination of acoustic impedance, longitudinal and lateral wave velocities for the characterization of the elastic microstructure of cortical bone," in *Proc. World Congr. Ultrason.*, Paris, France, 2003, pp. 321–324.
[32] J. M. Bland and D. G. Altman, "Statistical methods for assessing agreement between two methods of clinical measurement," *Lancet*, vol. 327, no. 8476, pp. 307–310, 1986.
[33] M. Granke *et al.*, "To what extent can cortical bone millimeter-scale elasticity be predicted by a two-phase composite model with variable porosity?" *Acta Biomaterialia*, vol. 12, pp. 207–215, Jan. 2015.
[34] O. Yousefian, R. D. White, Y. Karbalaeisadegh, H. T. Banks, and M. Müller, "The effect of pore size and density on ultrasonic attenuation in porous structures with mono-disperse random pore distribution: A two-dimensional *in-silico* study," *J. Acoust. Soc. Amer.*, vol. 144, no. 2, p. 709, 2018.
[35] Y. Karbalaeisadegh, O. Yousefian, G. Iori, K. Raum, and M. Müller, "Acoustic diffusion constant of cortical bone: Numerical simulation study of the effect of pore size and pore density on multiple scattering," *J. Acoust. Soc. Amer.*, vol. 146, no. 2, p. 1015, 2019.
[36] M. K. H. Malo *et al.*, "Longitudinal elastic properties and porosity of cortical bone tissue vary with age in human proximal femur," *Bone*, vol. 53, no. 2, pp. 451–458, 2013.
[37] J. S. Nyman, M. Granke, R. C. Singleton, and G. M. Pharr, "Tissue-level mechanical properties of bone contributing to fracture risk," *Current Osteoporosis Rep.*, vol. 14, no. 4, pp. 138–150, 2016.
[38] A. Wydra, E. Malyarenko, K. Shapoori, and R. G. Maev, "Development of a practical ultrasonic approach for simultaneous measurement of the thickness and the sound speed in human skull bones: A laboratory phantom study," *Phys. Med. Biol.*, vol. 58, no. 4, pp. 1083–1102, 2013.
[39] J. Schneider *et al.*, "*In vivo* measurements of cortical thickness and porosity at the proximal third of the tibia using guided waves: Comparison with site-matched peripheral quantitative computed tomography and distal high-resolution peripheral quantitative computed tomography," *Ultrasound Med. Biol.*, vol. 45, no. 5, pp. 1234–1242, 2019.
[40] D. Rohrbach *et al.*, "Distribution of mesoscale elastic properties and mass density in the human femoral shaft," *Connect Tissue Res.*, vol. 56, no. 2, pp. 120–132, 2015.
[41] M. Talmant *et al.*, "*In vivo* performance evaluation of bi-directional ultrasonic axial transmission for cortical bone assessment," *Ultrasound Med. Biol.*, vol. 35, no. 6, pp. 912–919, Jun. 2009.
[42] P. Moilanen *et al.*, "Discrimination of fractures by low-frequency axial transmission ultrasound in postmenopausal females," *Osteoporosis Int.*, vol. 24, no. 2, pp. 723–730, 2013.
[43] W. P. Olszynski *et al.*, "Multisite quantitative ultrasound for the prediction of fractures over 5 years of follow-up: The Canadian multicentre osteoporosis study," *J. Bone Mineral Res.*, vol. 28, no. 9, pp. 2027–2034, 2013.

Huong Nguyen Minh (M'19) was born in Berlin, Germany, in 1994. She received the B.Sc. and M.Sc. degrees in medical physics from the Martin Luther University of Halle-Wittenberg, Halle, Germany, in 2015 and 2018, respectively. She is currently pursuing the Ph.D. degree with the Berlin Brandenburg Center for Regenerative Therapies, Charité—Universitätsmedizin Berlin, Berlin.

Ms. Nguyen Minh became a member of the International Bone Ultrasound Society in 2018 and a member of the European Society of Biomechanics in 2019. She was a recipient of the Gustav-Mie-Bachelor-Award for her achievements during the bachelors in 2015.

Juan Du (M'13) was born in Hebei, China, in 1987. She received the B.Sc. degree in control, detection, and navigation from Beihang University, Beijing, China, in 2009, and the M.Sc. and Ph.D. degrees in electrical engineering from the University of Minnesota, Twin Cities, Minneapolis, MN, USA, in 2012 and 2016, respectively.

From 2014 to 2015, she was with the Department of Research and Development, Medtronic, Inc., Minneapolis, developing algorithms for ECG signal processing, the graphic user interface for physicians, and performing ultrasound acoustic field simulation and transducer modeling and optimization, which resulted in four granted U.S. patents. From 2016 to 2018, she was a Postdoctoral Researcher with the Berlin Brandenburg Center for Regenerative Therapies, Charité—Universitätsmedizin Berlin Berlin, Germany. She is currently with Digital Endoscopy GmbH, Friedberg, Germany. Her research interests include ultrasound microvascular imaging, ultrasound acoustics, biomedical-related signal and image processing, DSP design and implementation, and medical device development.

Kay Raum (M'02) was born in Halle, Germany, in 1972. He received the Diploma and Ph.D. (Dr.rer.nat.) degrees in physics from the Martin Luther University of Halle-Wittenberg, Halle, in 1997 and 2002, respectively.

He was a Visiting Scholar with the Bioacoustics Research Laboratory, University of Illinois at Urbana–Champaign, Champaign, IL, USA, from 1995 to 1996. From 1997 to 2003, he was a Research Assistant with the Medical Faculty, Martin Luther University of Halle-Wittenberg. In 2004, he was a Postdoctoral Fellow with the French National Center of Scientific Research, Paris, France, and joined the Laboratoire d'Imagerie Paramétrique, Sorbonne University Pierre and Marie Curie Campus, Paris, France. In 2006, he became the Research Head of the Interdisciplinary Center for Musculoskeletal Diseases, Medical Department, Martin Luther University. In 2009, he was appointed as a Full Professor for engineering basis of regeneration with the Berlin Brandenburg Center for Regenerative Therapies, Charité—Universitätsmedizin Berlin, Berlin, Germany. He has authored over 75 original papers and several book chapters. His research interests include the development and applications of ultrasound and X-ray tomography in musculoskeletal research, diagnosis, and therapy.

Dr. Raum is a Founding Member and a Treasurer of the International Bone Ultrasound Society, a member of the Acoustical Society of America, the Bone Ultrasound Society, the German Society for Biomedical Technology (VDE-DGBMT), and the German Osteology Society. He is an Associate Editor of the journals *Ultrasound in Medicine and Biology* and *Ultrasonic Imaging*.